A Two-Stream LSTM-Based Backscattering Model at L-Band and S- Band for Dry Soil Surfaces Under Large Roughness Conditions

Dong Zhu ⓘ, Peng Zhao, Qiang Zhao ⓘ, Qing-Liang Li, Yu-Shi Zhang, and Li-Xia Yang ⓘ, *Member, IEEE*

Abstract—In this article, we report for the first time two radar measurements (*Ji Mo 2008* and *Min Qin 2009*) on natural soil surfaces under large roughness, which were conducted by the China Research Institute of Radiowave Propagation. The desired HH and VV polarization backscatter data were measured by a truck-mounted scatterometer, which operates at L-band and S-band (i.e., 1.34 and 3.2 GHz, respectively). Simultaneously to radar acquisitions, the ground-truth data related to the rms height, the correlation length, and the dielectric constant were collected. Discrepancies between the simulations of the advanced integral equation model (AIEM) and the radar data have indicated the inadequacy of the AIEM model under large roughness conditions. To address this limitation, a new two-stream long short-term memory–based network was developed to receive the radar and surface parameters, termed radar-surface network (RSNet). The proposed network was trained on a hybrid dataset consisting of 1) a simulated dataset generated based on the AIEM under a wide range of conditions and 2) the radar data reported in *Ji Mo 2008* and *Min Qin 2009* combined with those simulated to make the dataset more relevant to natural conditions. After training, extensive experiments were performed to evaluate the performance of the proposed backscatter model. Comparisons demonstrate that the predictions of RSNet are generally in good agreement with both simulations and measured data, in terms of magnitude and trend, thus demonstrating that the proposed model can yield trustworthy and high-quality backscatter estimations at L-band and S-band for dry soil surfaces under large roughness conditions.

Dong Zhu, Qiang Zhao, and Li-Xia Yang are with the Information Materials and Intelligent Sensing Laboratory of Anhui Province, Anhui University, Hefei 230601, China (e-mail: zhudongahu@163.com; chrischao22s@163.com; lixiayang@yeah.net).

Peng Zhao, Qing-Liang Li, and Yu-Shi Zhang are with the National Key Laboratory of Electromagnetic Environment, China Research Institute of Radiowave Propagation, Qingdao 266108, China (e-mail: zhaopeng.xd@foxmail.com; qlianglicrirp@sina.cn; zhang10695@126.com).

Digital Object Identifier 10.1109/JSTARS.2023.3343526

I. INTRODUCTION

U NDERSTANDING and modeling radar backscatter from bare soil surfaces play a significant role in target detection, ground classification, and remote sensing data interpretation. Radar measurements are the most straightforward and effective way to obtain backscatter data. Over the past few decades, many researchers have conducted various radar campaigns over bare soil surfaces. For example, Ulaby et al. [1] carried out two radar measurements on bare surfaces at Texas State University and Lawrence, Texas, during 1974–1975. These two experiments measured the backscattering coefficients from bare fields, with the incidence angles ranging from 0° to 80° at 1–8 GHz, and contributed significantly to the study of the surface scattering problems. In research work [2], Oh et al. made the polarimetric radar measurements for bare soil surfaces under a wide range of roughness and moisture conditions at L-band, C-band, and X-band with incidence angles varying from 10° to 70°. In recent years, the China Research Institute of Radiowave Propagation (CRIRP) has carried out radar measurements on various types of terrains (e.g., bare surfaces, grassland, and sea ice), and then accumulated a large amount of experimental data.

It is well known that radar data are essential for developing an accurate backscatter model. However, to create a database that is representative of all available conditions of natural soil surfaces using different radar configurations would require a huge time and manpower investment [10]. Thus, various models have been introduced to accurately analyze and interpret the backscatter behavior from bare surfaces [2], [3], [4], [5], [6], [7], [8], [9], [10], [11]. Looking through the outcomes of these studies, two principal groups of models have emerged. The first is theoretical models, such as the physical optics model, the geometrical optics model, and the small perturbation model. Reportedly, their applicability is limited [4], and they are not sufficient for most natural surfaces [6]. Afterward, with the objective of expanding their validity region, the integral equation model (IEM) [3], [4], and its derivatives improved IEM [7] and advanced IEM (AIEM) [8] were developed. Because of the high precision and low computational cost, those IEM-based models bring a new perspective to the simulations of surface scattering

problems [12], [13], [14], [15], [16]. However, the geometric properties of natural surfaces are rather difficult to characterize accurately with statistical models. On the other hand, limiting assumptions are more or less applied in the derivation of those theoretical models. For all these reasons, estimations of radar backscatter from natural surfaces are still not adequate when using theoretical models.

The second group is empirical (semi-empirical) models. Oh model [2] is considered to be the most widely used one. This model was developed with the objective of reproducing the backscatter from the soil surface and retrieving the surface parameters of interest. Good agreements were obtained with the experimental observations. In addition to the Oh model, Dubois et al. [5] presented a semi-empirical algorithm for modeling the radar backscatter of bare surfaces based on the scatterometer data. The deviations observed among the IEM simulations and the SAR data motivated Baghdadi et al. [11] to propose an empirical calibration of the IEM. In contrast to theoretical models, which require complex mathematical derivations, empirical models relate several fitted parameters obtained from specific radar observations. However, they are only applicable to the conditions under which those radar data were measured, and some of the models neglect one (or two) of the surface parameters (e.g., the role of the correlation length is not involved in the Oh model [2]). In research work [6], a large discrepancy (about 3.2 dB) was observed between two IEM simulations, which were conducted with the same rms height ($s = 0.5$ cm) and different correlation lengths ($l = 3$ and 8 cm) at $30°$. As a result, these empirical models suffer from significant restrictions.

Computer science is moving forward at a rapid pace, and the deep-learning (DL) approaches have brought a new perspective to various fields, especially for image classification [17], [18], [19], object detection [20], [21], and semantic segmentation [22], [23]. Due to their powerful capabilities, extensive efforts have been devoted to investigating the applicability of the DL-based methods to the field of electromagnetic [24], [25], [26], [27], [28], [29], [30], [31], [32], [33], [34]. In the early stage, researchers have been attempting to explore whether DL-based methods could be used in computational electromagnetic (CEM) [24], [25], [26], [27]. In [25], Yao et al. treated the conventional method of moments (MoM) matrix as the training dataset, and the artificial neural network training process became a conventional linear algebra MoM-solving process. This novel idea brings a new perspective to CEM. Similarly, our previous work [27] aimed to apply DL-based methods to the finite-difference time-domain simulations. As expected, DL methods achieved satisfactory accuracy. Recently, extensive work has been undertaken to find the use of DL-based methods to address the electromagnetic scattering problems [28], [29], [30], [31], [32], [33], [34]. For instance, Li et al. [29], for the first time, exploited the connection between DL-based methods and nonlinear inverse scattering problems. Numerical and experimental results revealed that the DL-based method outperforms remarkably conventional methods in terms of both image quality and computational time. In [33], Xiao et al. proposed a hybrid method that combines DL and experimental design to reproduce the monostatic radar cross section of the conducting target.

Numerical experiments were carried out to evaluate the accuracy and efficiency of the proposed method. All these outcomes serve as a novel path for solving electromagnetic scattering problems. However, until now, most of the research has focused on applying DL-based methods to develop an inversion algorithm to reproduce the parameters of interest [28], [29], [30], [31], [32], i.e., inverse problems, and few efforts have been reported to characterize the forward problems [33], [34]. Apparently, an accurate forward method can be guided to develop an effective retrieval algorithm.

The radar measurements (*Ji Mo 2008*, and *Min Qin 2009*) carried out by the CRIRP were reported for the first time in this article. Validation of the measured data was made based on the AIEM simulations. Motivated by the deviations observed between the AIEM simulations and the measured data under large roughness conditions, we propose a two-stream long short-term memory (LSTM)–based model to address this issue. First, a hybrid dataset, consisting of many sets of input parameters (i.e., the radar configurations and surface parameters) and corresponding backscattering coefficients with Gaussian random noise, was generated based on the radar data and the AIEM simulations. Second, we build a two-stream LSTM network (radar-surface network, termed RSNet) to receive the radar configurations and surface parameters and use them as the multiple inputs of the model. Concretely, several LSTM blocks are employed to exploit the features from the input parameters. Furthermore, a feature fusion layer is applied to motivate the network to focus on the discriminative features. The network ultimately ends with a cascaded fully connected (FC) layer that is responsible for prediction. In this way, the proposed RSNet can exploit and fuse the correlated features from the multiple inputs and has the capability to estimate the radar backscatter from soil surfaces.

The rest of this article is organized as follows. Section II presents the truck-mounted scatterometer and the experimental campaigns. Section III validates the applicability of AIEM simulations with radar data. Section IV illustrates the proposed two-stream LSTM-based backscattering model. The detailed comparisons are shown in Section V. Finally, Section VI concludes this article.

II. RADAR MEASUREMENTS

A. Truck-Mounted Scatterometer System

CRIRP developed a truck-mounted scatterometer system, namely CRIRPSCAT, as shown in Fig. 1. This system mainly comprises an antenna module, a vector network analyzer (VNA) and a servo module. The antenna module is equipped with six sets of antennas in different bands (i.e., L-band, S-band, C-band, X-band, Ku-band, and Ka-band). The computer unit is responsible for sending commands to the VNA to transmit signals through the antenna and then receive the echo signals from the receiving antenna for the desired data. The servo module includes a servo control unit and a servo motor and is mainly used to control the elevation angle of the antenna, which can collect the scattering echoes of point (or distributed) targets at different incidence angles. Table I lists the basic configurations

Fig. 1. Photograph of the truck-mounted scatterometer system.

TABLE I
CONFIGURATIONS OF THE CRIRPSCAT

Configuration	L	S
Center frequency (GHz)	1.34	3.2
Bandwidth (GHz)	0.1	0.2
Antenna gain (dB)	≥ 18	
Antenna beamwidth (°)	≥ 10	
Polarization	HH / VV	
Platform height (m)	14	

Fig. 2. Photograph of (a) calibrator and (b) measurement for noise background level.

Fig. 3. Locations of the campaigns. (a) *Ji Mo 2008* in Qingdao, Shandong, China. (b) *Min Qin 2009* in Wuwei, Gansu, China.

of CRIRPSCAT, e.g., the center frequency, bandwidth, and antenna gain.

The operating principle of the truck-mounted scatterometer system is defined as follows.

1) The VNA generates the signal of a given frequency, and then the signal is delivered to the transmission antenna via a feeder.
2) The polarization switch of the transmission antenna controls the polarization mode of the signal and then delivers the signal to the feed.
3) The antenna receives the scattering signals from the soil surface and transmits the signals through the feeder to the VNA.
4) Then, the VNA converts the received signals into a time domain, and based on the beamwidth and antenna height, one can calculate the irradiation area. Then, it filters out edge clutter signals and retains valid signals.
5) The signal is processed by the VNA and transformed from the time domain to the frequency domain to obtain the value of the reflected power over the irradiated area.

B. Radar Measurements

In general, the procedure of the radar measurement is broadly organized into the following parts.

1) Calibrating the scatterometer: The objective of calibration is to reduce the error of the scatterometer system and enhance the accuracy of the measurement. The calibration formula is as follows:

$$\sigma^s = \frac{P_r \sigma_0 R^4}{P_{r0} A R_0^4} \tag{1}$$

where σ^s represents the surface backscattering coefficient and σ_0 is the theoretical scattering cross-section of the calibrator. P_r

and P_{r0} are the power of the surface echo and the calibrator. R denotes the distance from the antenna to the ground, whereas R_0 is the distance from the antenna to the calibrator. A is the irradiation area. Note that the calibrator used in this experiment was a standard hollow metal sphere, as shown in Fig. 2.

1) Selecting the test sites. It is important to note that the location of the test sites should be representative and easy to measure.
2) Setting up the devices, e.g., computer unit and antenna system.
3) Changing the incidence angles (i.e., elevation angles of the antenna) over the range of interest.
4) Acquiring the radar data via the scatterometer system.
5) Changing the azimuth and repeating the procedure to collect more independent samples.

To achieve the backscatter data from soil surfaces under large roughness conditions, two radar campaigns were conducted by the CRIRP, namely *Ji Mo 2008*, and *Min Qin 2009*. The locations of radar campaigns are shown in Fig. 3.

Ji Mo 2008: This campaign took place from December 20 to 31, 2008. Three test sites, located at 36.586°N, 120.435°E in Qingdao, Shandong, China, with an average elevation of 42 m, were selected for measurements. This campaign was devoted to measuring the plowed fields with soft soil and large roughness. The width of each test site was approximately 40 m, whereas the length was approximately 200 m. The radar data were collected by the CRIRPSCAT, which operates at L-band and S-band (1.34, and 3.2 GHz, respectively) at incidence angles ranging from 20° to 80° with an interval of 5°.

Min Qin 2009: This campaign was commenced on April 14, 2009, and completed on June 10, 2009. During the experiment, the desired radar data were collected from four fields, located at 39.006°N, 103.562°E in Wuwei, Gansu, China, with an average

TABLE II
GROUND MEASUREMENTS OF THE *JI MO*

Surface	s (cm)	l (cm)	f (GHz)	ks	kl	ε_r
J1	3.8	43.6	1.34	1.07	12.24	(4.59, 0.56)
			3.2	2.55	29.22	(4.83, 0.96)
J2	3.2	30.6	1.34	0.90	8.59	(4.26, 1.00)
			3.2	2.14	20.51	(4.16, 1.09)
J3	2.5	36.0	1.34	0.70	10.10	(4.13, 0.58)
			3.2	1.68	24.13	(4.07, 0.70)

Fig. 4.   Photograph of a roughness profile with a 2.4-m-long needle profilometer and a 3-cm interval between needles.
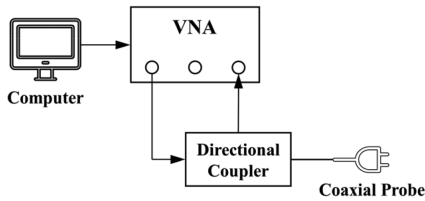

Fig. 5.   Diagram the system of dielectric constant measurement.

elevation of 1300 m. The radar configurations for this campaign were consistent with those of *Ji Mo 2008*, except for a slight change in the incidence angles, i.e., 25°–80° with an interval of 5°. Note that the test fields in *Min Qin 2009* were relatively smoother and drier than those in *Ji Mo 2008*.

C. Ground-Truth Measurements

For each test site, radar measurements were repeated (>16 times) at various azimuth angles to enhance the number of independent samples. Simultaneously to radar acquisitions, the ground-truth measurements were made over the corresponding soil surfaces. Soil roughness measurements were conducted using a 2.4-m-long needle profilometer with a 3-cm internal, as shown in Fig. 4. To achieve sufficient statistical precision, more than four profiles were recorded at each test field of those two campaigns. The rms height s and the correlation length l were estimated using the mean of all experimental correlation functions.

Fig. 5 shows the system for measuring the dielectric constant of the soil surfaces, which mainly consists of a computer, a VNA, a coaxial probe, etc. Based on transmission line theory, this system establishes a function between the dielectric constant and

measured values. It should be noted that the dielectric constant was measured at a depth of 4 cm over each test surface.

After preprocessing the measured data, a complete ground-truth dataset with large surface roughness conditions was established. Tables II and III summarize the ground-truth data for those two campaigns. For the full set of measurements, the rms height varies from 1.23 to 3.8 cm, and the correlation length ranges between 29.25 and 43.6 cm. Compared with other radar campaigns that have been reported [2], [6], all of the test fields reported in this article are at a large scale of roughness values, e.g., in [6], the rms height and correlation length vary from 0.36 to 1.58 cm and 1.5 to 16.9 cm, respectively. Therefore, the presented experiments are quite different from those in the literature [2], [6].

III. COMPARISON BETWEEN RADAR DATA AND AIEM SIMULATIONS

A. AIEM Model

In research work [8], modification of the IEM model [3] was made by removing a simplifying assumption in the spectral representation of the Green's function. Therefore, a more complete version of the IEM model was derived, namely AIEM. It is well known that the AIEM demonstrates significant improvements for single scattering problems over a wide range of roughness conditions [15], [16]. The general form of the AIEM is shown in the following equation:

$$\sigma_{pp}^s = \sigma_{pp}^k + \sigma_{pp}^{kc} + \sigma_{pp}^c = \frac{k^2}{2} \exp[-s^2(k_z^2 + k_{sz}^2)]$$

$$\times \sum_{n=1}^{\infty} \frac{s^{2n}}{n!} \left| I_{pp}^n \right|^2 W^{(n)}(k_{sx} - k_x, k_{sy} - k_y) \quad (2)$$

with

$$I_{pp}^n = (k_{sz} + k_z)^n f_{pp} e^{-s^2 k_z k_{sz}}$$

$$+ \frac{1}{4}\{(k_{sz} - q_1)^n F_{pp1}^{(+)} e^{-s^2(q_1^2 - q_1 k_{sz} + q_1 k_z)}$$

$$+ (k_{sz} - q_2)^n F_{pp2}^{(+)} e^{-s^2(q_2^2 - q_2 k_{sz} + q_2 k_z)}$$

$$+ (k_{sz} + q_1)^n F_{pp1}^{(-)} e^{-s^2(q_1^2 + q_1 k_{sz} - q_1 k_z)}$$

$$+ (k_{sz} + q_2)^n F_{pp2}^{(-)} e^{-s^2(q_2^2 + q_2 k_{sz} - q_2 k_z)}\}$$

$$+ \frac{1}{4}\{(k_z + q_1)^n F_{pp1}^{(+)} e^{-s^2(q_1^2 - q_1 k_{sz} + q_1 k_z)}$$

TABLE III
GROUND MEASUREMENTS OF THE *MIN QIN*

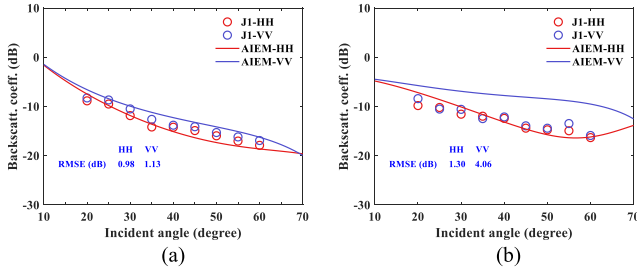| Surface	s (cm)	l (cm)	f (GHz)	ks	kl	ε_r
M1	2.04	36.7	1.34	0.57	10.30	(2.59, 0.57)
			3.2	1.37	24.60	(2.38, 0.55)
M2	1.51	29.25	1.34	0.42	8.21	(3.17, 1.31)
			3.2	1.01	19.60	(2.67, 0.85)
M3	1.99	36.38	1.34	0.56	10.21	(2.44, 0.20)
			3.2	1.33	24.38	(2.26, 0.21)
M4	1.23	39.13	1.34	0.35	10.98	(4.29, 2.99)
			3.2	0.82	26.23	(3.54, 1.86)

Fig. 6. Comparison of backscattering coefficients between AIEM simulations and the measured data of surface J1 for (a) L-band at 1.34 GHz and (b) S-band at 3.2 GHz.
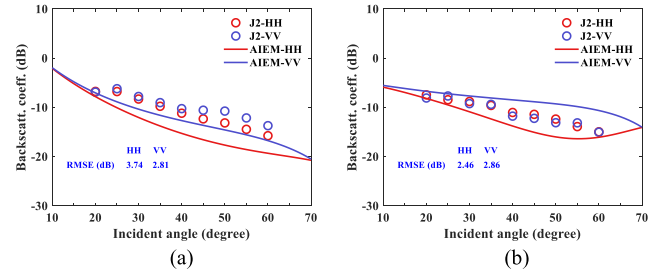

Fig. 7. Comparison of backscattering coefficients between AIEM simulations and the measured data of surface Surface J2 for (a) L-band at 1.34 GHz and (b) S-band at 3.2 GHz.

$$+ (k_z + q_2)^n F_{pp2}^{(+)} e^{-s^2(q_2^2 - q_2 k_{sz} + q_2 k_z)}$$
$$+ (k_z - q_1)^n F_{pp1}^{(-)} e^{-s^2(q_1^2 + q_1 k_{sz} - q_1 k_z)}$$
$$+ (k_z - q_2)^n F_{pp2}^{(-)} e^{-s^2(q_2^2 + q_2 k_{sz} - q_2 k_z)}\} \quad (3)$$

where $p = $ V and H stands for vertical or horizontal polarization, respectively. $k_x = k\sin\theta_i\cos\phi_i$, $k_y = k\sin\theta_i\sin\phi_i$, and $k_z = k\cos\theta_i$, and $k_{sx} = k\sin\theta_s\cos\phi_s$, $k_{sy} = k\sin\theta_s\sin\phi_s$, and $k_{sz} = k\cos\theta_s$. θ_i and θ_s represent the incidence angle and scattering angle, respectively. k is the wavenumber. For the sake of brevity, the remaining formulas are omitted here but can be referred to [8]. $W^{(n)}(\cdot)$ is the Fourier transform of the nth power of the normalized surface correlation function. In the case of natural surfaces, an exponential correlation function generally serves as a good match for most scenes [6]. Thus, we have

$$W^{(n)}(k_{sx} - k_x, k_{sy} - k_y) = \frac{l^2}{n^2}\left[1 + \left(\frac{2kl\sin\theta}{n}\right)^2\right]^{-1.5}. \quad (4)$$

B. Comparison Between the Radar Data and the AIEM

Figs. 6–12 show the comparisons of the AIEM simulations with the measured data. Particularly, surfaces J2 and M2 are used as examples to demonstrate the applicability of the AIEM in detail, and Fig. 13 shows the corresponding test fields.

1) Surface J2: It is seen in Table II that surface J2 represents a large roughness condition with $s = 3.2$ cm and $l = 30.6$ cm. Fig. 7
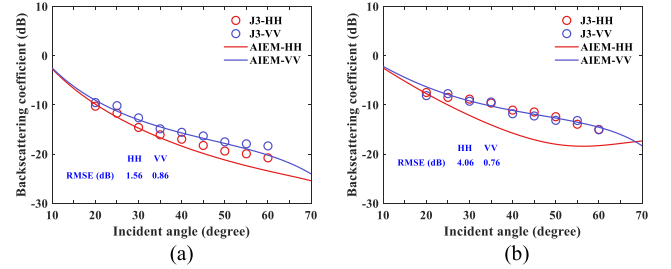

Fig. 8. Comparison of backscattering coefficients between AIEM simulations and the measured data of surface J3 for (a) L-band at 1.34 GHz and (b) S-band at 3.2 GHz.

illustrates the AIEM simulations compared with the measured data at 1.34 and 3.2 GHz for both HH and VV polarizations. It can be found in Fig. 7(a) that the simulated values of the AIEM, on the whole, capture the trend of the measured data, but fail to match the magnitude well. The root-mean-square errors (RMSE) for HH and VV polarizations are equal to 3.74 and 2.81 dB, respectively. As the frequency increases from 1.34 to 3.2 GHz (or ks increases from 0.9 to 2.14), the AIEM predictions show a large deviation from the measured data, especially at intermediate incidence angles (e.g., 40° and 50°), with overall RMSE values of 2.46 and 2.86 dB, respectively.

2) Surface M2: As observed in Table III, the rms height and correlation length of surface M2 are 1.51 and 29.25 cm, respectively, which is regarded as a relatively smooth condition among these two experiments. Fig. 10 shows the comparison of
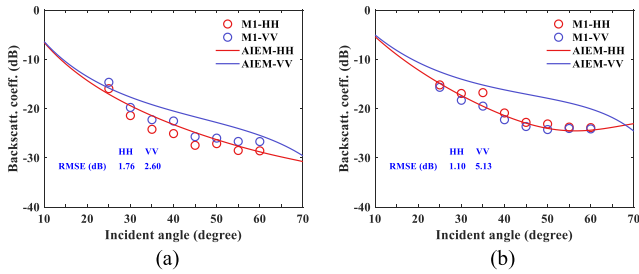
Fig. 9. Comparison of backscattering coefficients between AIEM simulations and the measured data of surface M1 for (a) L-band at 1.34 GHz and (b) S-band at 3.2 GHz.

Fig. 10. Comparison of backscattering coefficients between AIEM simulations and the measured data of surface M2 for (a) L-band at 1.34 GHz and (b) S-band at 3.2 GHz.
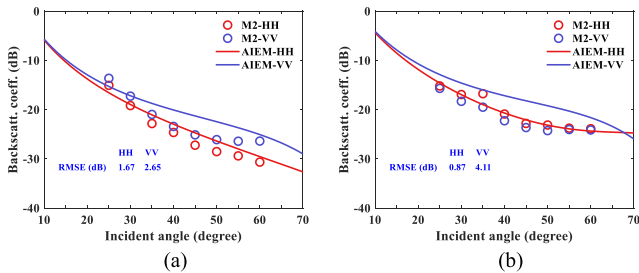

Fig. 11. Comparison of backscattering coefficients between AIEM simulations and the measured data of surface M3 for (a) L-band at 1.34 GHz and (b) S-band at 3.2 GHz.
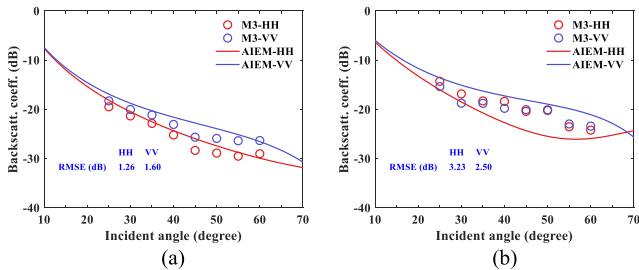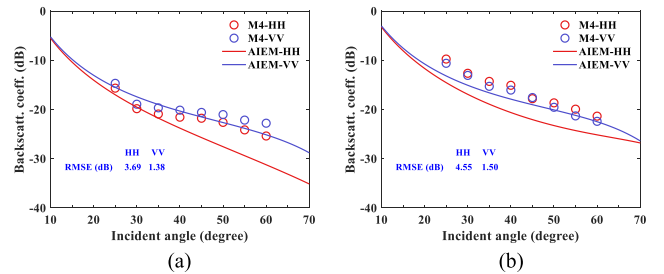

Fig. 12. Comparison of backscattering coefficients between AIEM simulations and the measured data of surface M4 for (a) L-band at 1.34 GHz and (b) S-band at 3.2 GHz.

Fig. 13. Photograph of the test fields. (a) Surface J2, with $s = 3.2$ cm and $l = 30.6$ cm. (b) Surface M2, with $s = 1.51$ cm and $l = 29.25$ cm.

scattering gradually increases with the roughness increases; and 2) the correlation length assessment may be inaccurate, as it is not only the least accurate parameter but also the most difficult to measure [10].

IV. MODEL DEVELOPMENT

In Section III, the discrepancies between the AIEM simulations and the radar data under large roughness conditions were demonstrated. Motivated by this issue, we propose a new DL-based backscatter model using the simulated data and the measured data.

A. LSTM-Based Backscatter Model for Soil Surfaces

According to the derivation of the AIEM, the soil backscatter acts as a function of the radar configurations (i.e., frequency, incidence angles, and polarizations) and the surface parameters (i.e., rms height, correlation length, and dielectric constant). Without loss of generality, we assume that $R(\cdot)$ and $S(\cdot)$ denote the nonlinear mappings of the radar and surface parameters, respectively, then an explicit expression is given by

$$\left[\sigma_{\text{HH}}^0, \sigma_{\text{VV}}^0\right] = \text{AIEM}\left\{R(f, \theta_i); S(s, l, \varepsilon_r)\right\}. \quad (5)$$

With reference to (2) and (5), we can observe a complex nonlinear relationship between the soil backscatter and the input parameters. Reportedly, DL-based networks work as a powerful tool to solve nonlinear relationships due to the presence of the activation function [36], [37]. On the other hand, all the parameters in (5) contribute to the backscatter through a coupled way, which indicates that the interconnections between the parameters are also required to be considered. Moreover, according to (5), each parameter vector can be regarded as a set of orderly sequences.

the AIEM predictions and the measured data for surface M2. In this case, the AIEM simulations perform better than those for surface J2. It is observed from Fig. 10 that the AIEM simulations for HH polarization are in good agreement with the measured data, with lower RMSEs of 1.67 and 0.87 dB for both L-band and S-band. However, for VV polarization, there is an obvious discrepancy between the AIEM and the measured data. The RMSEs are greater than those for HH polarization.

It is reported that the validity domain of such an IEM-based algorithm is generally limited to $ks < 3$ [4], [35]. As seen in Tables II and III, the ks values of surfaces J2 and M2 are both within their validity range. However, the results shown in Figs. 7 and 10 reveal the limited applicability of the AIEM in correctly estimating the soil surface backscatter under large roughness conditions. In practice, these limitations may be related to the following reasons: 1) the AIEM used in this article performs the single scattering mechanism, whereas the effect of multiple
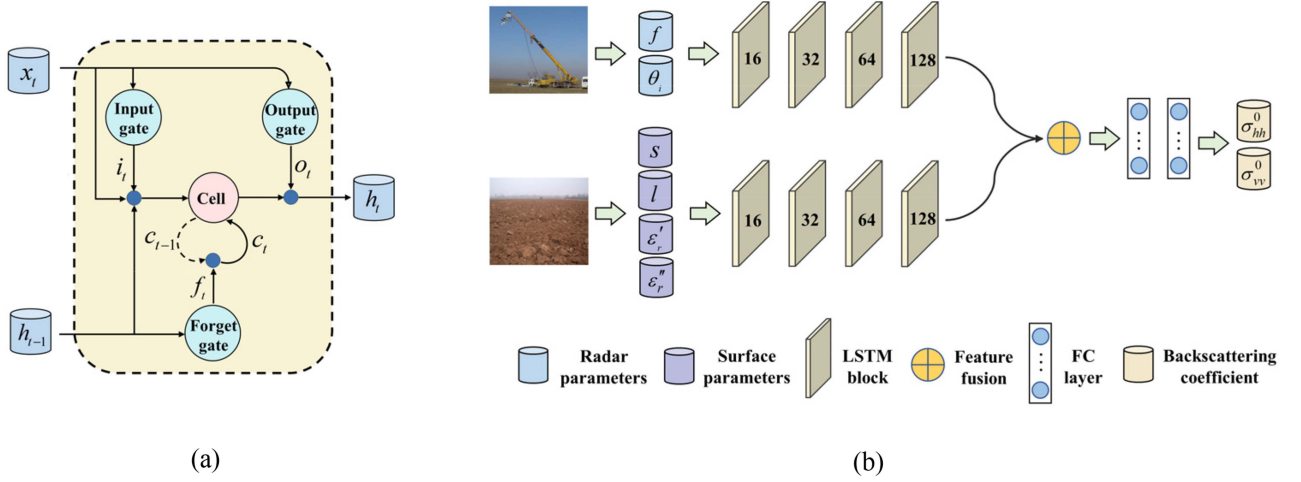
Fig. 14. Diagram of (a) LSTM block and (b) proposed RSNet.

Among fundamental DL networks, LSTM neural network is one of the most powerful networks for processing sequential inputs [38], [39], [40]. In view of this, the LSTM network is well-suited for the backscatter estimation of soil surfaces. To justify these considerations, we build a two-stream LSTM-based backscatter model, RSNet, to tackle the inadequacy of the AIEM simulations under large roughness conditions.

As shown in Fig. 14(a), the LSTM block consists of four units, namely an input gate, a forget gate, a memory cell, and an output gate. The input gate controls the data flow from the network to the memory cell, whereas the cell is applied to record and store the internal state of information. Simultaneously, the forget gate can learn to reset the previous state when the stored information is no longer needed [36].

The general formulas of the input gate, forget gate, and output gate are given by

$$i_t = \delta(W_{ix}x_t + W_{ih}h_{t-1} + b_i) \tag{6}$$

$$f_t = \delta(W_{fx}x_t + W_{fh}h_{t-1} + b_f) \tag{7}$$

$$o_t = \delta(W_{ox}x_t + W_{oh}h_{t-1} + b_o). \tag{8}$$

The expression of the memory cell is given as

$$c_t = f_t \odot c_{t-1} + i_t \odot \tanh(W_{cx}x_t + W_{ch}h_{t-1} + b_c). \tag{9}$$

Finally, we have the hidden layer update formula

$$h_t = o_t \odot \tanh(c_t) \tag{10}$$

where x_t and h_t are the input and final output, respectively. $\delta(\cdot)$ denotes the sigmoid activation function and $\tanh(\cdot)$ represents the hyperbolic tangent activation function. W is the weight, whereas b is the bias (for convenience, we ignore subscripts). $\odot$ denotes the elementwise product.

Fig. 14(b) illustrates the diagram of the proposed two-stream RSNet. As the name suggests, this model contains two identical subnetworks that take the radar configurations and the surface parameters as the multiple inputs, as listed in (5). We assume

that the inputs of these two streams are x_R and x_S, so we have

$$x_R = [f, \theta_i]^T, x_S = [s, l, \varepsilon'_r, \varepsilon''_r]^T. \tag{11}$$

Then, the features between elements of the input sequences are exploited by several LSTM blocks in each stream. Note that in Fig. 14(b), the bold digits within LSTM blocks represent the numbers of hidden neurons, which are set to 16, 32, 64, and 128. After acquiring these desired features, a linear fusion strategy is utilized to concatenate the output of each subnetwork. Finally, the fused feature maps are entered into the cascaded FC layers. For the sake of illustration, we simplify the process represented by (6)–(10) as $L\mathrm{stm}(\cdot)$ Therefore, we have

$$o_c = L\mathrm{stm}(x_R) \oplus L\mathrm{stm}(x_S) = \{h_1, \ldots h_m : h_1, \ldots, h_n\}. \tag{12}$$

Concretely, h_m and h_n are the outputs of the subnetworks, with m, and n equal to the number of the hidden neurons of the last LSTM block, 128, in this article. o_c represents the output of the fusion layer. $\oplus$ represents the linear fusion operation. A fusion layer is able to concatenate a list of inputs and return a single tensor that is the concatenation of all inputs. Our principle in applying this strategy is to force the subnetworks to contribute as much as possible to the predicted results by exploiting more representative feature maps along the layers of each stream. Then, the final output of RSNet can be written as

$$[\sigma^0_{\mathrm{HH}}, \sigma^0_{\mathrm{VV}}]^T = \delta(W_{fc}o_c + b_{fc}) \tag{13}$$

where W_{fc} and b_{fc} denote the weight and bias of the FC layer, respectively.

B. Dataset and Network Setup

DL-based methods strongly depend on both the quantity and quality of the training data. It is undeniable that the AIEM is a well-established model for estimating soil backscatter under many scene conditions [15], [16]. It is, therefore, suitable for generating an extensive training set.

Table IV summarizes the ranges and sampling intervals of the radar and surface parameters. It should be noted that, due

Parameters	Range	Interval
f (GHz)	$1-4$	0.5
Θ_i (°)	$20-60$	5
s (cm)	$0.5-2$	0.5
l (cm)	$5-25$	10
ε_r'	$2.5-10.5$	2
ε_r''	$0.5-4.5$	2

to the limited radar data available to us, we set the frequency within the L-band and S-band (i.e., 1–4 GHz with a 0.5 GHz interval), and the incidence angles between 20° and 60° with a 5° interval. As observed in Section III, the performance of the AIEM simulations is significantly suppressed as the roughness increases. Therefore, the surface parameters are accordingly set in a reasonable range, e.g., 0.5–2 cm for s with a 0.5 cm interval and 5–25 cm for l with a 10 cm interval. In addition, to approximate the backscattering coefficient of soil surface under natural conditions, we added a zero mean Gaussian random noise with a standard deviation of ±0.5 dB to the values produced by the AIEM.

As shown in Table IV, we can conclude that the simulated dataset mainly represents the smooth or slightly rough cases, which is insufficient for developing a DL-based model to address the objective of this article. Alternatively, the reported radar measurements provide the probable roughness conditions of the natural surfaces under large roughness conditions. It is noteworthy at this point that, some of the radar data and the corresponding ground-truth data were constructed as the natural dataset, including surfaces J2, J3, M1, M2, and M4. The remaining measured data (surfaces J1 and M3, known as CRIRPSCAT data) were used for validation, which will be discussed in Section IV-C. After combination, a total of 11 424 sets of data were obtained which are referred to as the hybrid dataset. For this study, 70% of the hybrid dataset was randomly selected as the training set, 20% as the validation dataset, and the rest as the test set.

The proposed RSNet is mainly implemented with the Keras framework, and end-to-end trained on an NVIDIA GTX 1650Ti GPU laptop. As indicated in (5), the input dimension of these two streams is set to 2 and 4, respectively. During the training process, the mean-squared error loss function is optimized by the adaptive moment estimation (Adam) [41] with momentum. To reduce the computational complexity, the backscattering coefficients are normalized to [0, 1]. The momentum is fixed to 0.9, and the weight decay is set to 1e-4. The learning rate during the training process is equal to 0.001. The batch size and epoch are set to 64 and 1000, respectively.

Moreover, two statistical indices are utilized to quantitatively verify the performance of the proposed model, namely the RMSE, and the bias. Their expressions are shown as follows:

$$\text{RMSE} = \sqrt{\frac{1}{m}\sum_{i=1}^{m}(p_i - y_i)^2} \qquad (14)$$
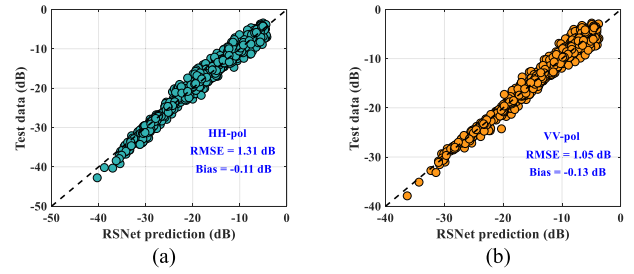

Fig. 15. Correlation of backscattering coefficients between RSNet predictions and test data for (a) HH and (b) VV polarization.
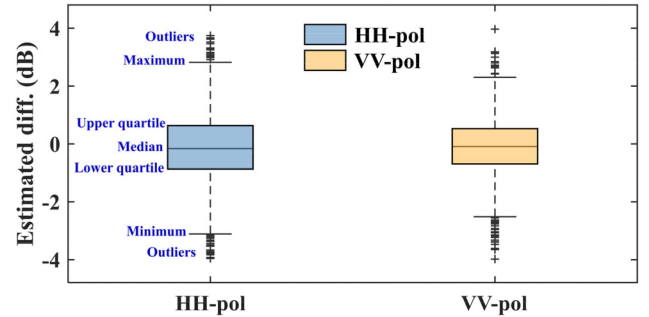

Fig. 16. Box plot of the estimated differences between model predictions and the test data for both HH and VV polarization.

$$\text{Bias} = \frac{1}{m}\sum_{i=1}^{m}(p_i - y_i) \qquad (15)$$

where p_i and y_i are the ith predicted result and ground truth, respectively, and m is the number of data points.

V. EXPERIMENTAL RESULTS

A. Comparison With Test Set

The objective of this section is to evaluate the performance of the proposed model on the test set. The correlation plots for HH and VV polarizations are depicted in Fig. 15. The predicted values of RSNet agree well with the test data. Furthermore, the detailed quantitative indices also indicate that the proposed model can provide high precision in predicting the backscattering coefficients with overall RMSE and Bias values of 1.31 and -0.11 dB, respectively, for HH polarization, and 1.05 and -0.13 dB, respectively, for VV polarization. Fig. 16 presents the box plot of the estimated differences among the model predictions and the measured data for HH, and VV polarization. The box plot is a statistical diagram that shows the dispersion of data, and the statistical meanings are shown in blue font in Fig. 16. Despite the fact that there are several outliers up to 4 dB, the overall median values of the estimated differences generally vary in the range of 0–1 dB, thus exhibiting the good performance of the proposed RSNet.

To visually show the performance of RSNet, two examples are presented in Fig. 17. It is observed that the predicted backscattering coefficients are close to those of the AIEM simulations in terms of both magnitude and trend, with low RMSE and Bias values. As ks increases, slight discrepancies are observed at smaller
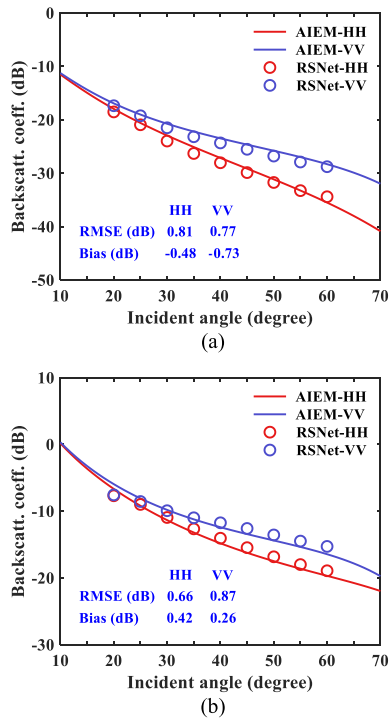
Fig. 17. Comparison of backscattering coefficients between RSNet predictions and validation data with (a) V1: $f = 1.5$ GHz, $s = 0.5$ cm, $l = 10$ cm, and $\varepsilon_r = (4.50.5)$ and (b) V2: $f = 2.5$ GHz, $s = 1.5$ cm, $l = 20$ cm, and $\varepsilon_r = (6.52.5)$.

incidence angles (e.g., 20°). As the incidence angle becomes larger, the discrepancies are gradually reduced as expected.

In summary, the aforementioned outcomes strongly support the point that LSTM can characterize the relationship between the input parameters and soil backscatter, suggesting the capability of the proposed RSNet in estimating the soil backscatter.

B. Comparison With POLARSCAT Data

In this section, we verify the robustness of the proposed model with the experimental measurements under relatively smooth surface conditions. POLARSCAT data [2], acquired by a truck-mounted polarimetric scatterometer [42], cover a wide range of roughness and moisture conditions and are well suited for evaluating the model performance [15], [43]. Three different surfaces, namely S1, S2, and S3, are used in this article. The radar data were acquired at L-band (1.5 GHz) at incidence angles ranging from 20° to 50° for both HH and VV polarizations. The ground truth data were simultaneously obtained from the corresponding surfaces with s ranging from 0.32 to 1.12 cm and l varying from 8.4 to 9.9 cm, as listed in Table V.

Fig. 18 shows the correlation plots of the measured data and RSNet predictions for the selected surfaces. It can be clearly observed that the RSNet predictions are very close to the 1:1 line, suggesting a strong intensive correlation between the model predictions and the measured data. The statistical indices also reveal the good accuracy of the RSNet model in predicting backscattering coefficients under natural conditions, with low

TABLE V
RADAR AND SURFACE PARAMETERS OF POLARSCAT

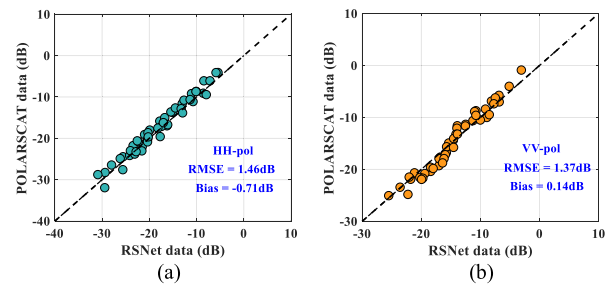| Surface	f (GHz)	s (cm)	l (cm)	ε_r
S1		0.4	8.4	(7.99, 2.02)
S2	1.5	0.32	9.9	(5.85, 1.46)
S3		1.12	8.4	(7.70, 1.95)

Fig. 18. Correlation of backscattering coefficients between RSNet predictions and POLARSCAT data for (a) HH and (b) VV polarization.

TABLE VI
STATISTICAL INDICES BETWEEN RSNET PREDICTIONS, AIEM SIMULATIONS, AND POLARSCAT DATA

Surface	Freq. (GHz)	Pol.	RSNet RMSE	RSNet Bias	AIEM RMSE	AIEM Bias
S1		HH	0.90	-0.24	1.58	-1.14
		VV	1.02	0.28	1.09	-0.49
S2	1.5	HH	1.59	-0.19	3.77	-3.20
		VV	1.02	0.41	2.75	-2.52
S3		HH	0.54	0.03	0.36	0.10
		VV	1.38	0.52	2.41	1.76

RMSE and Bias values of 1.46 and −0.71 dB for HH polarization, and 1.37 and 0.14 dB for VV polarization, respectively.

To further demonstrate the performance of RSNet, we present a comparison of the values generated by the AIEM and RSNet for those three surfaces, as shown in Fig. 19. For surfaces S1 and S3, a good agreement is observed, over the range of intermediate incidence angles (i.e., 20° to 50°), whereas for surface S2, the AIEM predictions have large deviations from the measured data at 40°, with a maximum value of 5 dB for HH polarization, and 4 dB for VV polarization. As expected, RSNet predictions closely match the angular magnitude and trend of the POLARSCAT data for all these cases. To quantitatively assess the capacity of the proposed model, we compute the statistical indices among the AIEM simulations and RSNet predictions, and the detailed values are listed in Table VI. It can be observed that, among the three surfaces, RSNet achieves a better performance than the AIEM, in terms of the RMSE and Bias. Based on these results, it can be concluded that the proposed model is more suitable than AIEM for predicting the backscattering coefficient of natural surfaces under relatively smooth conditions. This could be explained by the fact that LSTM can easily learn the nonlinear relationship between the parameters and the radar backscatter.
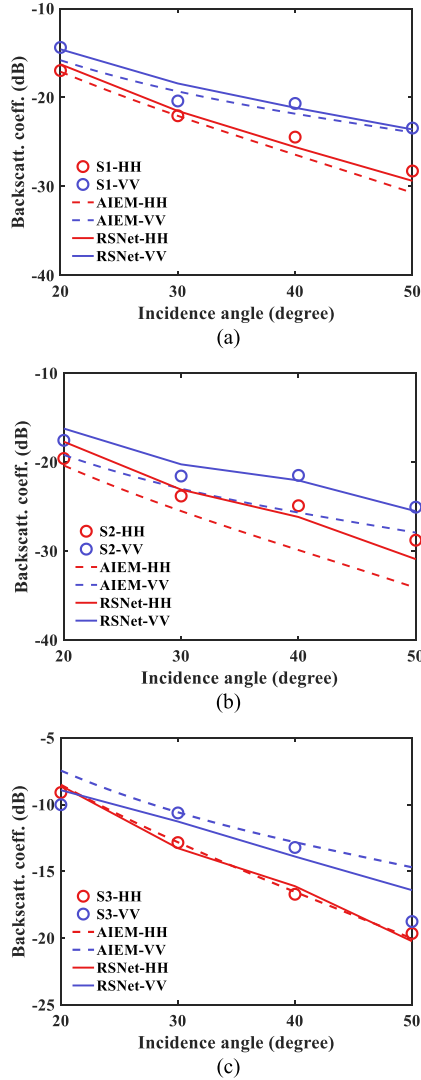
Fig. 19. Comparison of backscattering coefficients between AIEM simulations, POLARSCAT data, and RSNet predictions with (a) S1: $s = 0.4$ cm, $l = 8.4$ cm, and $\varepsilon_r = (7.99, 2.02)$, (b) S2: $s = 0.32$ cm, $l = 9.9$ cm, and $\varepsilon_r = (5.85, 1.46)$, and (c) S3: $s = 1.12$ cm, $l = 8.4$ cm, and $\varepsilon_r = (7.70, 1.95)$ for 1.5 GHz.

C. Comparison With CRIRPSCAT Data

CRIRPSCAT data (i.e., surfaces J1 and M3), as mentioned in Section IV-A, were not chosen to feed into the dataset. Therefore, we will employ these data, for validation purposes, in this section. As presented in Tables II and III, surfaces J1 and M3 are different from POLARSCAT data in terms of the surface parameters, which can be utilized to examine the generalization capability of the proposed model under large roughness conditions.

Figs. 20 and 21 depict the correlation plots of RSNet, the AIEM simulations, and measured data. Note that surface J1 refers to the roughest surface among these experiments, with $s = 3.8$ cm and $l = 43.6$ cm, whereas the rms height and correlation length of surface M3 are 1.99 cm and 36.38 cm, respectively, representing a relatively rough condition. A very close agreement is observed with the 1:1 line for RSNet
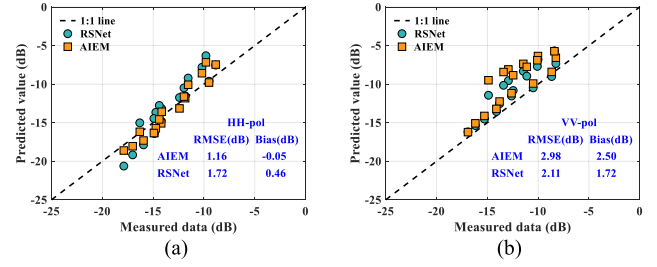

Fig. 20. Correlation of backscattering coefficients between model predictions and the measured data for surface J1. (a) HH polarization. (b) VV polarization.
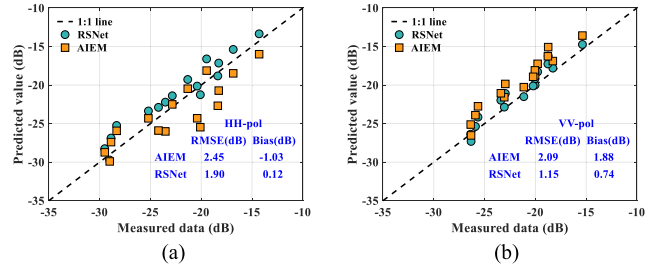

Fig. 21. Correlation of backscattering coefficients between model predictions and the measured data for surface M3. (a) HH polarization. (b) VV polarization.

TABLE VII
STATISTICAL INDICES BETWEEN RSNET PREDICTIONS, THE AIEM
SIMULATIONS, AND CRIRP DATA

Surface	Freq. (GHz)	Pol.	RSNet		AIEM	
			RMSE	Bias	RMSE	Bias
J1	1.34	HH	1.53	-0.72	0.98	-0.42
		VV	0.80	0.64	1.13	1.04
	3.2	HH	1.88	1.64	1.31	0.32
		VV	2.87	2.80	4.06	3.97
M3	1.34	HH	2.04	1.73	1.26	0.89
		VV	0.70	0.17	1.60	1.37
	3.2	HH	1.75	-1.49	3.23	-2.95
		VV	1.48	1.30	2.49	2.40

predictions in Fig. 20, with favorable RMSE values of 1.72 dB for HH polarization and 2.11 dB for VV polarization, respectively. Fig. 21 then shows the comparison for surface M3. A very strong correlation between the predicted values by RSNet and the measured data is again observed. Concerning the Bias, the detailed values indicate that the proposed model overestimates the backscattering coefficient for both surfaces, i.e., surface J1 with 0.46 dB for HH polarization and 1.72 dB for VV polarization, respectively, and surface M3 with 0.12 dB for HH polarization and 0.74 dB for VV polarization, respectively. This may be explained by the fact that the samples of larger roughness conditions within the dataset are insufficient for the model to learn the intrinsic connections adequately.

Figs. 22 and 23 demonstrate the angular behavior of RSNet predictions, the AIEM simulations, and the measured data, whereas the corresponding statistical indices are listed in Table VII. From Fig. 22(a), the values reproduced by RSNet and the AIEM, on the whole capture the angular trends of the measured data well, whereas the performance of the proposed model is slightly worse over the incidence angle range of 50° to

Fig. 22. Comparison of backscattering coefficients between the AIEM simulations, CRIRPSCAT data, and RSNet predictions with $s = 3.8$ cm and $l = 43.6$ cm for (a) L-band and (b) S-band.
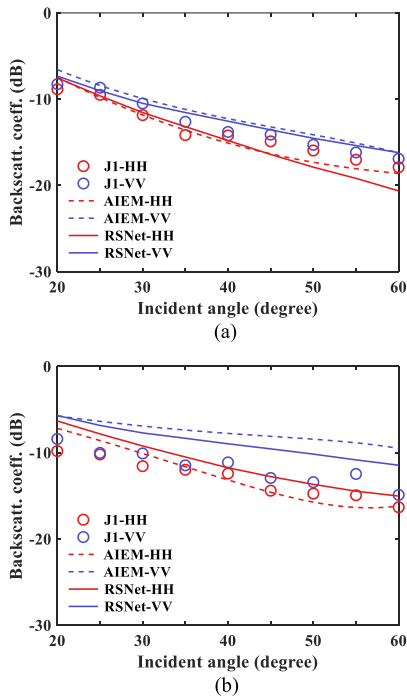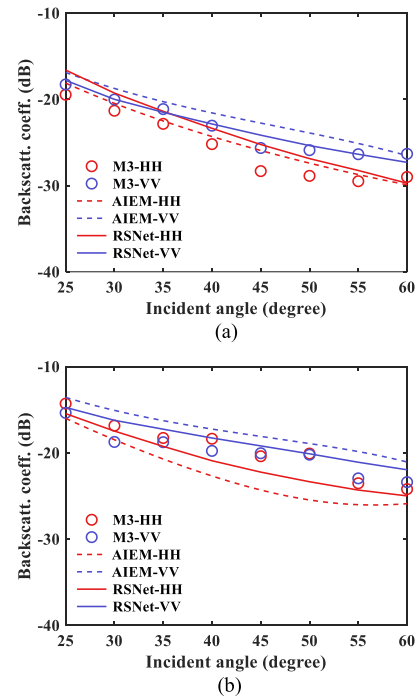

Fig. 23. Comparison of backscattering coefficients between the AIEM simulations, CRIRPSCAT data, and RSNet predictions with $s = 1.99$ cm and $l = 36.38$ cm for (a) L-band and (b) S-band.

$60°$ for HH polarization, with a higher RMSE value of 1.53 dB. In the case of surface M3 [see Fig. 23(a)], both RSNet and AIEM predictions match well with the measured data for HH polarization, whereas for VV polarization, RSNet predictions perform better than the AIEM simulations. As the frequency (or ks) increases, the precision of the proposed model significantly outperforms that of the AIEM. With reference to Fig. 22(b), we see that both the AIEM and RSNet provide similar accuracy on the measured data for HH polarization, but in the case of VV polarization, the AIEM gives rise to obvious separation over the angular range with higher RMSE and Bias values of 4.06 and 3.97 dB, respectively. Some deviations between the AIEM simulations and the measured data are also observed in Fig. 23(b) with RMSE and Bias values greater than those of RSNet predictions. It is concluded that the proposed model outperforms the AIEM in estimating the backscattering coefficient under large roughness conditions.

D. Sensitivity Analysis

As previously mentioned, a total of 11 424 sets of data were obtained, containing 11 340 samples simulated by the AIEM and a very limited amount of 84 sets of measured data. This indicates that the measured data only represent a very small proportion of the training dataset, i.e., less than 1%. To provide a convincing justification, a comparison experiment was made to assess the sensitivity of the model accuracy to the amount of real radar data.

The procedure of the comparison experiment is broadly organized into the following parts. First, the ground-truth data
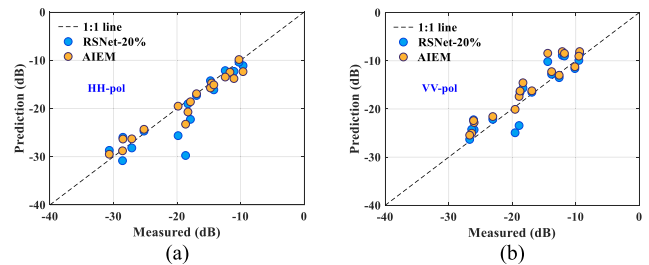

Fig. 24. Correlation plot between RSNet and AIEM predictions on validation data. RSNet was trained with 20% of the real radar data and simulated dataset. (a) HH polarization. (b) VV polarization.

were paired with the corresponding radar backscatter data. Second, 20% of those paired data were randomly selected as the validation dataset. Third, the remaining data (i.e., 80%) were proportionally incorporated with the simulated dataset to train the model. Finally, the results on the validation dataset were recorded and shown in Figs. 24–27. The corresponding RMSEs are listed in Table VIII. It can be seen from these figures that, with the real radar data proportionally increasing, the model predictions gradually converge to the 1:1 line, and the RMSEs of RSNet were reduced as expected. It also can be found in Table VIII that for the cases of HH polarization, the predicted errors of RSNet perform better than the AIEM simulations when the percentage of the radar data exceeds 50%, whereas the percentage is 30% for VV polarization. Those outcomes reveal that the hybrid dataset, even if it contains merely 1% of the real radar data, can give an improvement in accuracy to the networks.
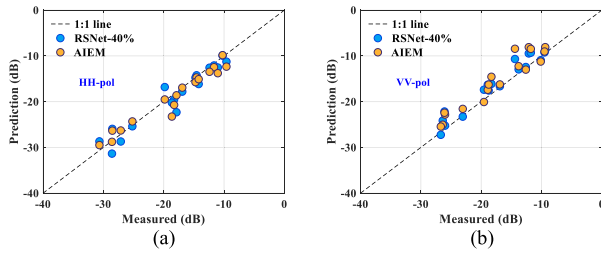
Fig. 25. Correlation plot between RSNet and AIEM predictions on validation data. RSNet was trained with 40% of the real radar data and simulated dataset. (a) HH polarization. (b) VV polarization.

Fig. 26. Correlation plot between RSNet and AIEM predictions on validation data. RSNet was trained with 60% of the real radar data and simulated dataset. (a) HH polarization. (b) VV polarization.

Fig. 27. Correlation plot between RSNet and AIEM predictions on validation data. RSNet was trained with 80% of the real radar data and simulated dataset. (a) HH polarization. (b) VV polarization.
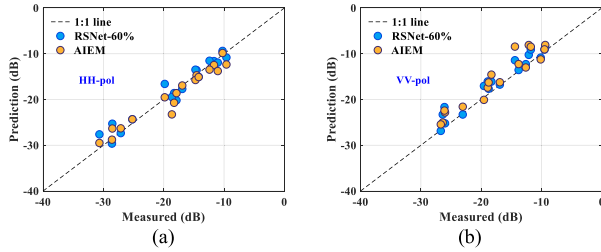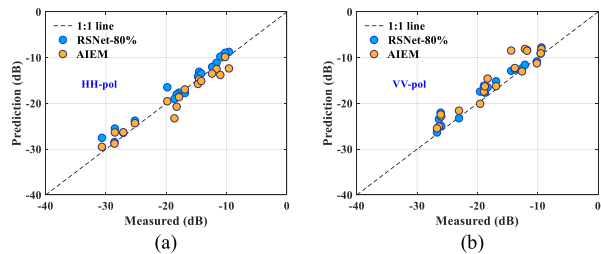
TABLE VIII
COMPARISON OF THE PREDICTIONS ON THE VALIDATION DATASET

Percentage (%)	RMSE (dB)			
	RSNet		AIEM	
	HH	VV	HH	VV
10	3.12	2.38		
20	3.35	2.64		
30	1.89	2.41		
40	1.88	1.95	1.73	2.59
50	1.72	2.03		
60	1.59	2.00		
70	1.43	1.82		
80	1.52	1.91		

VI. CONCLUSION

Understanding the radar backscatter from natural surfaces requires a suitable model that is capable of predicting backscattering coefficients close to those observations by radar. Since the validity region of the AIEM covers a wide range of roughness

values, it was used to validate the measured data collected by the CRIRPSCAT. However, deviations between the AIEM simulations and the measured data have shown the inadequacy of this model under large roughness conditions. Taking this into account, a new LSTM-based backscatter model (RSNet) was developed and then trained on the hybrid dataset, which consists of a simulated dataset produced by the AIEM and the experimental data acquired by the scatterometer. We conducted extensive experiments to verify the feasibility and performance of the LSTM-based model. First, the proposed RSNet was validated by comparing its predictions with those obtained with the AIEM. Good agreement is shown between these models, and the overall RMSE value is within 1.31 dB. Next, we compared the model predictions with POLARSCAT data. The outcomes show that the model predictions are closely related to the radar measurements under relatively smooth conditions, persistently justifying the robustness of this model. Then, comparisons between the proposed DL-based model and CRIRPSCAT data under large roughness conditions were performed. As expected, the RSNet predictions significantly outperform the AIEM simulations and the average RMSEs are estimated to be 1.77 dB for surface J1 and 1.49 dB for surface M3, respectively. Finally, the sensitivity of the model accuracy to the amount of real radar data was made. The results revealed that limited real radar data can indeed bring an improvement to the model performance. All these promising outcomes will serve as a new path for further developing a retrieval algorithm.

It is concluded from this article that the proposed RSNet can provide a reasonable estimation of the radar backscatter from natural surfaces under large roughness conditions. However, the ranges of related parameters proposed in Table IV were not reached high values, especially for the rms height and real part of the dielectric constant. Therefore, a few additional comments on the limits of validity of the proposed model we would like to make. First, to ensure the accuracy of the dataset simulated by AIEM, the values of rms height were set to 0.5∼2 cm. Meanwhile, the reported measured data (i.e., surfaces J2, J3, M1, M2, and M4) were used to cover the large roughness conditions. As a result, the proposed model works well within those scope of roughness. Second, due to the limited data available to us, the real part of the dielectric constant also did not go to high values, which means the proposed model is applicable to those soil surfaces under relatively dry conditions. Finally, it would be advisable to calibrate the proposed model on other radar measurements to broaden its validity in more generalized conditions.

REFERENCES

[1] F. T. Ulaby, R. K. Moore, and A. K. Fung, *Microwave Remote Sensing: Active and Passive*. Norwood, MA, USA: Artech House, 1986.
[2] Y. Oh, K. Sarabandi, and F. T. Ulaby, "An empirical model and an inversion technique for radar scattering from bare soil surfaces," *IEEE Trans. Geosci. Remote Sens.*, vol. 30, no. 2, pp. 370–381, Mar. 1992.
[3] A. K. Fung, Z. Li, and K. S. Chen, "Backscattering from a randomly rough dielectric surface," *IEEE Trans. Geosci. Remote Sens.*, vol. 30, no. 2, pp. 356–369, Mar. 1992.
[4] A. K. Fung, *Microwave Scattering and Emission Models and Their Applications*. Norwood, MA, USA: Artech House, 1994.

[5] P. C. Dubois, J. Van Zyl, and T. Engman, "Measuring soil moisture with imaging radars," *IEEE Trans. Geosci. Remote Sens.*, vol. 33, no. 4, pp. 915–926, Jul. 1995.

[6] M. Zribi and M. Dechambre, "A new empirical model to retrieve soil moisture and roughness from C-band radar data," *Remote Sens. Environ.*, vol. 84, no. 1, pp. 42–52, 2002.

[7] A. K. Fung, W. Y. Liu, K. S. Chen, and M. K. Tsay, "An improved IEM model for bistatic scattering from rough surfaces," *J. Electromagn. Waves Appl.*, vol. 16, no. 5, pp. 689–702, 2002.

[8] K. S. Chen, T.-D. Wu, L. Tsang, Q. Li, J. Shi, and A. K. Fung, "Emission of rough surfaces calculated by the integral equation method with comparison to three-dimensional moment method simulations," *IEEE Trans. Geosci. Remote Sens.*, vol. 41, no. 1, pp. 90–101, Jan. 2003.

[9] A. K. Fung and K. S. Chen, *Microwave Scattering and Emission Models for Users*. Norwood, MA, USA: Artech House, 2010.

[10] N. Baghdadi, I. Gherboudj, M. Zribi, and M. R. Sahebi, "Semi-empirical calibration of the IEM backscattering model using radar images and moisture and roughness field measurements," *Int. J. Remote Sens.*, vol. 25, no. 18, pp. 3593–3623, Sep. 2004.

[11] N. Baghdadi, N. Holah, and M. Zribi, "Calibration of the integral equation model for SAR data in C-band and HH and VV polarizations," *Int. J. Remote Sens.*, vol. 27, no. 4, pp. 805–816, 2006.

[12] Q. Li, J. Shi, and K. S. Chen, "A generalized power law spectrum and its applications to the backscattering of soil surfaces based on the integral equation model," *IEEE Trans. Geosci. Remote Sens.*, vol. 40, no. 2, pp. 271–280, Feb. 2002.

[13] A. K. Fung and K. S. Chen, "An update on the IEM surface backscattering model," *IEEE Geosci. Remote Sens. Lett.*, vol. 1, no. 2, pp. 75–77, Apr. 2004.

[14] N. Baghdadi, E. Saba, M. Aubert, M. Zribi, and F. Baup, "Evaluation of radar backscattering models IEM, Oh, and Dubois for SAR data in X-band over bare soils," *IEEE Geosci. Remote Sens. Lett.*, vol. 8, no. 6, pp. 1160–1164, Nov. 2011.

[15] J. Zeng, K.-S. Chen, H. Bi, T. Zhao, and X. Yang, "A comprehensive analysis of rough soil surface scattering and emission predicted by AIEM with comparison to numerical simulations and experimental measurements," *IEEE Trans. Geosci. Remote Sens.*, vol. 55, no. 3, pp. 1696–1708, Mar. 2017.

[16] Y. Yang, K.-S. Chen, L. Tsang, and L. Yu, "Depolarized backscattering of rough surface by AIEM model," *IEEE J. Sel. Topics Appl. Earth Observ. Remote Sens.*, vol. 10, no. 11, pp. 4740–4752, Nov. 2017.

[17] A. Krizhevsky, I. Sutskever, and G. E. Hinton, "ImageNet classification with deep convolutional neural networks," in *Proc. Adv. Neural Inf. Process. Syst.*, 2012, pp. 1097–1105.

[18] K. Simonyan and A. Zisserman, "Very deep convolutional networks for large-scale image recognition," in *Proc. 3rd Int. Conf. Learn. Representation*, 2015, pp. 1–14.

[19] K. He, X. Zhang, S. Ren, and J. Sun, "Deep residual learning for image recognition," in *Proc. IEEE Int. Conf. Comput. Vis. Pattern Recognit.*, 2016, pp. 770–778.

[20] R. Girshick, J. Donahue, T. Darrell, and J. Malik, "Rich feature hierarchies for accurate object detection and semantic segmentation," in *Proc. IEEE Int. Conf. Comput. Vis. Pattern Recognit.*, 2014, pp. 580–587.

[21] S. Ren, K. He, R. Girshick, and J. Sun, "Faster R-CNN: Towards real-time object detection with region proposal networks," *IEEE Trans. Pattern Anal. Mach. Intell.*, vol. 39, no. 6, pp. 1137–1149, Jun. 2017.

[22] J. Long, E. Shelhamer, and T. Darrell, "Fully convolutional networks for semantic segmentation," in *Proc. IEEE Int. Conf. Comput. Vis. Pattern Recognit.*, 2015, pp. 3431–3440.

[23] L.-C. Chen, Y. Zhu, G. Papandreou, F. Schroff, and H. Adam, "Encoder-decoder with atrous separable convolution for semantic image segmentation," in *Proc. Eur. Conf. Comput. Vis.*, 2018, pp. 833–851.

[24] H. M. Yao, L. Jiang, H. H. Zhang, and W. E. I. Sha, "Machine learning methodology review for computational electromagnetics," in *Proc. Int. Appl. Comput. Electromagn. Soc. Symp.*, 2019, pp. 1–4.

[25] H. M. Yao, L. J. Jiang, and Y. W. Qin, "Machine learning based method of moments (ML-MoM)," in *Proc. IEEE Int. Symp. Antennas Propag., USNC/URSI Nat. Radio Sci. Meeting*, 2017, pp. 973–974.

[26] H. M. Yao and L. Jiang, "Machine-learning-based PML for the FDTD method," *IEEE Antennas Wireless Propag. Lett.*, vol. 18, no. 1, pp. 192–196, Jan. 2019.

[27] D. Zhu, Q. Zhao, Y. Bo, W. Chen, and L. Yang, "Application of deep learning in FDTD method," in *Proc. Int. Symp. Antennas, Propag. EM Theory*, 2021, pp. 1–3.

[28] Z. Wei and X. Chen, "Deep-learning schemes for full-wave nonlinear inverse scattering problems," *IEEE Trans. Geosci. Remote Sens.*, vol. 57, no. 4, pp. 1849–1860, Apr. 2019.

[29] L. Li, L. G. Wang, F. L. Teixeira, C. Liu, A. Nehorai, and T. J. Cui, "DeepNIS: Deep neural network for nonlinear electromagnetic inverse scattering," *IEEE Trans. Antennas Propag.*, vol. 67, no. 3, pp. 1819–1825, Mar. 2019.

[30] K. Xu, L. Wu, X. Ye, and X. Chen, "Deep learning-based inversion methods for solving inverse scattering problems with phaseless data," *IEEE Trans. Antennas Propag.*, vol. 68, no. 11, pp. 7457–7470, Nov. 2020.

[31] Y. Zhou, Y. Zhong, Z. Wei, T. Yin, and X. Chen, "An improved deep learning scheme for solving 2-D and 3-D inverse scattering problems," *IEEE Trans. Antennas Propag.*, vol. 69, no. 5, pp. 2853–2863, May 2021.

[32] D. Zhu, Q. Zhao, L. Yang, Y. Bo, and W. Chen, "Multi-model fusion approach for electromagnetic inverse scattering problems," *IET Microw., Antennas Propag.*, vol. 16, no. 9, pp. 610–616, Jun. 2022.

[33] D. Xiao, L. Guo, W. Liu, and M. Hou, "Efficient RCS prediction of the conducting target based on physics-inspired machine learning and experimental design," *IEEE Trans. Antennas Propag.*, vol. 69, no. 4, pp. 2274–2289, Apr. 2021.

[34] H. H. Zhang, H. M. Yao, L. Jiang, and M. Ng, "Fast full-wave electromagnetic forward solver based on deep conditional convolutional autoencoders," *IEEE Antennas Wireless Propag. Lett.*, vol. 22, no. 4, pp. 779–783, Apr. 2023.

[35] M. Zribi, N. Baghdadi, and C. Guerin, "Analysis of surface roughness heterogeneity and scattering behavior for radar measurements," *IEEE Trans. Geosci. Remote Sens.*, vol. 44, no. 9, pp. 2438–2444, Sep. 2006.

[36] S. Hochreiter and J. Schmidhuber, "Long short-term memory," *Neural Comput.*, vol. 9, no. 8, pp. 1735–1780, Nov. 1997.

[37] J. Schmidhuber, F. Gers, and D. Eck, "Learning nonregular languages: A comparison of simple recurrent networks and LSTM," *Neural Comput.*, vol. 14, no. 9, pp. 2039–2041, Sep. 2002.

[38] L. Ma et al., "Sea clutter amplitude prediction using a long short-term memory neural network," *Remote Sens.*, vol. 11, no. 23, 2019, Art. no. 2826.

[39] C. Wang, X. Liu, J. Pei, Y. Huang, Y. Zhang, and J. Yang, "Multiview attention CNN-LSTM network for SAR automatic target recognition," *IEEE J. Sel. Topics Appl. Earth Observ. Remote Sens.*, vol. 14, pp. 12504–12513, 2021.

[40] H. Wan, X. Tian, J. Liang, and X. Shen, "Sequence-feature detection of small targets in sea clutter based on bi-LSTM," *IEEE Trans. Geosci. Remote Sens.*, vol. 60, 2022, Art. no. 4208811.

[41] Y. LeCun et al., "Backpropagation applied to handwritten zip code recognition," *Neural Comput.*, vol. 1, no. 4, pp. 541–551, Dec. 1989.

[42] M. A. Tassoudji, K. Sarabandi, and F. T. Ulaby, "Design consideration and implementation of the LCX polarimetric scatterometer (POLARSCAT)," Radiation Lab., Univ. Michigan, Ann Arbor, MI, USA, Tech. Rep. 022486-T-2, 1989.

[43] Y. Wang et al., "Multi-parameter inversion of AIEM by using Bi-directional deep neural network," *Remote Sens.*, vol. 14, no. 14, 2022, Art. no. 3302.

Dong Zhu received the B.E. degree in electronic information engineering and the M.E. degree in electromagnetic and microwave technology in 2016 and 2019, respectively, from Anhui University, Hefei, China, where he is currently working toward the Ph.D. degree in electronic information engineering.

His research interests include deep learning, land clutter simulation, and electromagnetic inverse scattering.

Peng Zhao received the B.S. and M.S. degrees in radio physics from Xidian University, Xi'an, China, in 2010 and 2013, respectively. He is currently working toward the Ph.D. degree in radio physics with the School of Physics, Xidian University, Xi'an, China.

He is currently a Senior Engineer with the China Research Institute of Radiowave Propagation, Qingdao, China. His research interests include land-sea clutter measurements, clutter modeling and analysis, and terrain-like clutter prediction methods.

Qiang Zhao received the B.S. degree in electronic information science and technology from Xidian University, Xi'an, China, in 2016, and the M.S. degree in radio physics from the China Research Institute of Radiowave Propagation, Qingdao, China, in 2019. He is currently working toward the Ph.D. degree in electromagnetic and microwave technology with the Department of Electronic Information Engineering, Anhui University, Hefei, China.

His research interests include electromagnetics, atmospheric propagation, and electromagnetic scattering.

Yu-Shi Zhang received the Ph.D. degree in radio physics from Xidian University, Xi'an, China, in 2014.

He is currently a Researcher with the China Research Institute of Radiowave Propagation, Qingdao, China. His research interests include sea clutter experiment systems and sea clutter modeling.

Li-Xia Yang (Member, IEEE) received the B.S. degree in physics from Hubei University, Wuhan, China, in 1997, and the Ph.D. degree in radio physics from Xidian University, Xi'an, China, in 2007.

From 2010 to 2011, he was a Post-Doctoral Research Fellow with the ElectroScience Laboratory, The Ohio State University, Columbus, OH, USA. Since 2010, he has been an Associate Professor with the Communication Engineering Department, Jiangsu University, Zhenjiang, China. From 2015 to 2016, he was a Visiting Scholar with the Institute of Space Science, The University of Texas at Dallas, Richardson, TX, USA. Since 2016, he has been a Professor, a Ph.D. Supervisor, and the Chairperson with the Communication Engineering Department, Jiangsu University. He is currently with the Information Materials and Intelligent Sensing Laboratory of Anhui Province, Anhui University, Hefei, China, and the Key Laboratory of Intelligent Computing and Signal Processing, Anhui University. He is the author of 1 book and more than 100 articles and the owner of 10 inventions and holds 4 patents. His research interests include wireless communication techniques, radio sciences, computational electromagnetic and antenna theory, and design in wireless communication systems.

Dr. Yang is a member of the Editor Board of the Chinese Journal of Radio Science.

Qing-Liang Li was born in Henan, China, in 1963. He received the Ph.D. degree in electromagnetic fields and microwave technology from Xidian University, Xi'an, China, in 1998.

Since 2016, he has been the Chief Scientist with China Electronics Technology Group Corporation, Beijing, China. His research interests include numerical methods for electromagnetic fields, electromagnetic scattering, and sea clutter characteristics.

Dr. Li was the recipient of the first-class reward of National Technology Improvements.